Journal of Systems Engineering and Electronics
Vol. 34, No. 4, August 2023, pp.894 – 905

A high frequency vibration compensation approach for ultra-high resolution SAR imaging based on sinusoidal frequency modulation Fourier-Bessel transform

CHEN Siyu, WANG Yong*, and CAO Rui

School of Electronics and Information Engineering, Harbin Institute of Technology, Harbin 150001, China

Abstract: Ultrahigh resolution synthetic aperture radar (SAR) imaging for ship targets is significant in SAR imaging, but it suffers from high frequency vibration of the platform, which will induce defocus into SAR imaging results. In this paper, a novel compensation method based on the sinusoidal frequency modulation Fourier-Bessel transform (SFMFBT) is proposed, it can estimate the vibration errors, and the phase shift ambiguity can be avoided via extracting the time frequency ridge consequently. By constructing the corresponding compensation function and combined with the inverse SAR (ISAR) technique, well-focused imaging results can be obtained. The simulation imaging results of ship targets demonstrate the validity of the proposed approach.

Keywords: synthetic aperture radar (SAR), high frequency vibration compensation, sinusoidal frequency modulation Fourier-Bessel transform (SFMFBT).

DOI: 10.23919/JSEE.2023.000059

1. Introduction

Synthetic aperture radar (SAR) can acquire high-quality imaging results independent of time and weather, thus making it an effective tool in civil and military fields [1−3]. Recently, its development has entered into a new stage with the application of ultrahigh resolution SAR imaging [4,5].

Nonetheless, even tiny phase errors can seriously affect image quality in a SAR system [6]. Since the wavelength of ultrahigh resolution SAR is small, the high frequency vibration error cannot be ignored, and the conventional motion compensation algorithm fail to perform. Even tiny high frequency vibration error will lead to serious defocused images [7]. Therefore, the research for high frequency vibration compensation is necessary.

Existing researches have established the signal model to research the high frequency vibration [8−15]. Generally speaking, the vibration can be divided into harmonic vibration, jitter vibration, tremor vibration, random vibration, etc. We usually use the harmonic vibration to model the high frequency vibration error, and other vibrations can be decomposed via harmonic vibration [16].

So far, there has been a lot of researches on the compensation algorithms for high frequency vibration. A parameter estimation method based on the short-time Fourier transform (STFT) was proposed [8,9,17], but its estimation accuracy is poor. In [10,18], a parameter estimation approach based on the wavelet transform was proposed to compensate for the vibration error. The estimation accuracy of the algorithm is high and the computational complexity of the algorithm is low. The discrete sinusoidal frequency modulation transform (DSFMT) optimized via the simulated annealing (SA) algorithm was proposed in [11]. It can estimate vibration parameters successfully. In [12], the fractional Fourier transform (FrFT) was proposed to estimate the vibration error, which has high estimation accuracy. In [13], the local FrFT (LFrFT) was used to obtain the vibration acceleration by estimating the instantaneous chirp rate, thereby estimating the vibration frequency consequently. In [14,19], the sinusoidal frequency modulation Fourier transform (SFMFT) was proposed to reconstruct the vibration error, and the phase shift ambiguity correction is discussed. The full aperture was decomposed into sub-apertures in [15], and the phase error of each sub-aperture was estimated via the entropy theorem. In [20], the vibration error was estimated via the inverse Radon transform, but the disadvantage of this algorithm is its low accuracy of multi-component signal parameter estimation. The discrete FrFT (DFrFT) was used to perform the

Manuscript received January 04, 2022.
*Corresponding author.
This work was supported by the National Natural Science Foundation of China (61871146) and the Fundamental Research Funds for the Central Universities (FRFCU5710093720).

parameter estimation [21,22]. The experimental results demonstrate that the algorithm can process the vibration with two frequencies.

The researches discussed above all used parameter estimation methods, and some researches have studied the non-parametric estimation methods. An estimation method via the autofocus algorithm was introduced in [23], which simplifies the vibration estimation process. In [24], all range slices were aligned for the motion compensation. The non-parametric estimation method avoids the direct estimation of the vibration parameters and reduces the computation burden, but its estimation accuracy is lower than that of the parametric estimation method.

Nevertheless, a few problems still need to be solved. The high frequency vibration error can introduce sinusoidal modulation phase error into the received signals. Hence, extracting the phase error is the precondition for the vibration error estimation. When the amplitude of phase error exceeds range $[-\pi,\pi]$, phase shift ambiguity occurs. Thus, how to more accurately extract the phase error has always been the focus of many literature. Moreover, the accuracy of the high frequency vibration parameter estimation directly affects the image quality. Therefore, the sinusoidal frequency modulation Fourier-Bessel transform (SFMFBT) in conjunction with the time frequency ridge extraction and parameter space projection is proposed to estimate and compensate for the vibration error. Through the time frequency ridge extraction, the phase shift ambiguity can be avoided. Then, the SFMFBT and the parameter space projection are employed for the vibration parameter estimation. In addition, the SFMFBT algorithm is more precise and effective in comparison with the DSFMT algorithm in [11].

In the remainder of this paper, we present the high frequency vibration model in Section 2. The high frequency vibration compensation approach based on the SFMFBT is proposed in Section 3. Then, the validity of the proposed method is proved via the ship target simulation experiment in Section 4. In Section 5, conclusions are drawn.

2. Model of ultrahigh resolution SAR

2.1 High frequency vibration model of the platform

As expressed previously, the high frequency vibration cannot be ignored in the ultrahigh resolution SAR system. Therefore, the platform vibration model is established first.

If the signal satisfies Dirichlet condition, it can be decomposed into the Fourier series [25]. Actually, the actual vibrations all meet the Dirichlet condition, so the platform vibration error can be defined as

$$\Delta R = \sum_{n=1}^{+\infty} A_n \sin(2\pi f_n t_m + \varphi_n) \tag{1}$$

where A_n, f_n, and φ_n are the vibration amplitude, frequency, and initial phase respectively; t_m represents the slow time. When the absolute value of the product of vibration frequency and synthetic aperture duration is equal or greater than 1, platform vibration is considered as high frequency vibration.

2.2 Signal model

The imaging geometric model of the airborne ultrahigh resolution SAR is shown in Fig. 1, which works at the vertical side-looking strip mode with velocity of V. The height of the platform is H, and the ideal trajectory of the platform is along the X axis. The dotted line represents the actual trajectory.

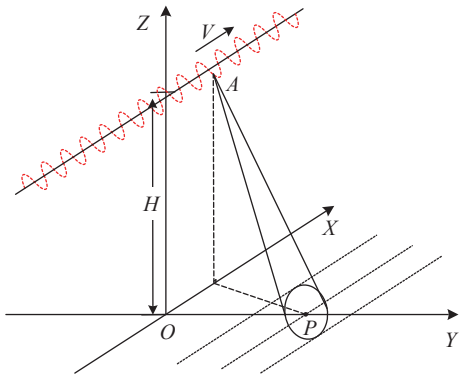

Fig. 1 Ultrahigh resolution SAR imaging geometric model

Suppose that radar transmits a chirp signal. After demodulation, the radar return is denoted as

$$s(\tau_f, t_m) = \eta' \exp\left(\mathrm{j}\pi k_f \left(\tau_f - \frac{2R(t_m)}{\mathrm{c}}\right)^2 - \mathrm{j}\frac{4\pi}{\lambda} R(t_m)\right) \tag{2}$$

where τ_f means the fast time, η' means the signal amplitude, $R(t_m)$ is the slant range from the platform to the target point, c is the speed of light, λ denotes the transmitted wavelength, $k_f = B/T_p$ means the frequency modulation rate, B is the bandwidth, and T_p is the pulsewidth.

The range-Doppler (RD) technique is used in this paper. Then, the range compression is performed on (2), and the received signal can be expressed as

$$s(\tau_f, t_m) = \eta \,\mathrm{sinc}\left[\pi B\left(\tau_f - \frac{2R(t_m)}{\mathrm{c}}\right)\right] \cdot \exp\left[-\mathrm{j}\frac{4\pi}{\lambda} R(t_m)\right] \tag{3}$$

where η is the signal magnitude after range compression.

From Fig. 1, we can see that the coordinates of the

scatterer P and the actual antenna phase center (APC) are $(0, y_p, 0)$ and $(\Delta R_x + Vt_m, \Delta R_y, \Delta R_z + H)$ respectively, where ΔR_x, ΔR_y, and ΔR_z are the high frequency vibration components of the X, Y, and Z axes respectively. Then, the slant range between the APC and the scatterer can be indicated as

$$R(t_m) = \left[(\Delta R_x + Vt_m)^2 + (\Delta R_y - y_p)^2 + (H + \Delta R_z)^2\right]^{\frac{1}{2}}. \quad (4)$$

In addition, vibration error along the X axis has little effect on the imaging result [26]. In this case, the Taylor expansion is used to further process (4), which can be rewritten as

$$\Delta R = -\frac{y_p \Delta R_y}{R_p} + \frac{H \Delta R_z}{R_p}, \quad (5)$$

$$R(t_m) \approx R_p + \frac{(Vt_m)^2}{2R_p} + \Delta R, \quad (6)$$

where $R_p = \left[y_p^2 + H^2\right]^{\frac{1}{2}}$ is the range from the platform to the scene center.

As we know, $\Delta R/\mathrm{c} \approx 0$. Then, after the range cell migration correction (RCMC), the received signal can be expressed as

$$s(\tau_f, t_m) = \eta \operatorname{sinc}\left[\pi B\left(\tau_f - \frac{2R_p}{\mathrm{c}}\right)\right] \cdot \exp\left\{\mathrm{j}\pi k_a t_m^2 - \mathrm{j}\frac{4\pi R_p}{\lambda} - \mathrm{j}\frac{4\pi \Delta R}{\lambda}\right\} \quad (7)$$

where $k_a = -2V^2/(\lambda R_p)$ indicates the Doppler frequency modulation rate.

Then a reference function H_r is constructed:

$$H_r = \exp\left\{-\mathrm{j}\pi k_a t_m^2\right\}. \quad (8)$$

By multiplying (7) and (8), a sinusoidal frequency modulation (SFM) signal is acquired:

$$\Omega' = \eta \operatorname{sinc}\left[\pi B\left(\tau_f - \frac{2R_p}{\mathrm{c}}\right)\right] \cdot \exp\left\{-\mathrm{j}\frac{4\pi R_p}{\lambda}\right\}, \quad (9)$$

$$s(\tau_f, t_m) = \Omega' \cdot \exp\left\{-\mathrm{j}\frac{4\pi \Delta R}{\lambda}\right\} = \Omega' \cdot \exp\left\{-\mathrm{j}\frac{4\pi}{\lambda}\left[\sum_{n=1}^{+\infty} A_n \sin(2\pi f_n t_m + \varphi_n)\right]\right\}, \quad (10)$$

where A_n, f_n, and φ_n are the vibration amplitude, frequency, and initial phase respectively.

The high frequency vibration error introduces sinusoidal modulation phase error into received signals, which has a severe impact on the ultrahigh resolution SAR imaging. From (10), we can see that the amplitude of the sinusoidal modulation phase error depends on the ratio of the vibration amplitude to the transmitted wavelength. The wavelength of the traditional X-band SAR is around 3 cm, while the high frequency vibration amplitude is usually several millimeters [27]. Therefore, for conventional SAR systems, the vibration error is almost negligible. Nevertheless, the wavelength of the ultrahigh resolution SAR is commonly in the millimeter or submillimeter range, which is equal to or even smaller than the vibration amplitude. Consequently, the vibration error can no longer be ignored for the ultrahigh resolution SAR imaging.

Next, we construct the compensation function by parameter estimation:

$$H_{\mathrm{ref}} = \exp\left\{\mathrm{j}\frac{4\pi}{\lambda}\left[\sum_{n=1}^{+\infty} \hat{A}_n \sin\left(2\pi \hat{f}_n t_m + \hat{\varphi}_n\right)\right]\right\} \quad (11)$$

where $\hat{A}_n$, $\hat{f}_n$, and $\hat{\varphi}_n$ are the estimation of A_n, f_n, and φ_n respectively.

Then, we can compensate for the vibration error and obtain the well-focused imaging results.

3. High frequency vibration parameters estimation method of the platform based on SFMFBT

3.1 Phase shift ambiguity

In order to compensate the phase error, the error needs to be extracted for estimation first. Through extracting the imaginary part after taking the natural logarithm of the SFM signal, we can obtain the measurements of the phase in (10). Nevertheless, the phase measurements are only possibly between $-\pi$ and π, therefore, when the amplitude of the real phase in the SFM signal exceeds range $[-\pi, \pi]$, the algorithm in [19] is used to correct the phase shift ambiguity.

However, we cannot get the phase accurately when the phase difference between adjacent phase points is more than π, and the algorithm in [19] does not perform well at low signal-to-noise ratio (SNR). Therefore, we use the STFT-based method to extract the error. The STFT is employed to obtain the time frequency representation of a certain range cell, and the time frequency ridge is extracted for the parameter estimation as

$$s_{\mathrm{ridge}}(t) = \begin{cases} \arg\max\limits_{\omega} S_{\mathrm{STFT}}(t, \omega), & t \in (0, T) \\ 0, & \text{else} \end{cases} \quad (12)$$

where ω is the frequency, $S_{\mathrm{STFT}}(t, \omega)$ is the result of STFT. Since STFT avoid taking the natural logarithm of

the SFM signal, the phase shift ambiguity can be avoided via STFT and the phase of the SFM signal can be obtained precisely.

3.2 High frequency vibration parameter estimation of the platform

The premise of the vibration error compensation is the vibration parameter estimation. We model a basic SFM signal to illustrate the steps of parameter estimation first:

$$s(t)=\sigma_0\exp\left\{\mathrm{j}\left[\frac{A_0}{f_0}\sin(2\pi f_0 t+\theta_0)\right]\right\} \tag{13}$$

where σ_0 is the amplitude of the SFM signal, A_0, f_0, and θ_0 are the maximum frequency offset, the modulation frequency, and the modulation initial phase of the SFM signal respectively.

For the signal in (13), the time frequency ridge extracted by STFT is $A_0\cos(2\pi f_0 t+\theta_0)$. Consequently, the time frequency ridge cannot be used to directly compensate for the vibration error. Therefore, the SFMFBT in conjunction with the parameter space projection is used for the parameter estimation. Then, the compensation function can be constructed via the estimated values to finish the vibration error compensation.

(i) Modulation frequency estimation

We estimate the modulation frequency based on the SFMFBT in [28]. The SFMFBT separates the SFM signal using the Fourier-Bessel transform, and the k-resolution parameter is introduced to improve frequency resolution. The SFMFBT is defined as

$$S_a(\zeta)=\mathrm{SFMFBT}[s(t)]=\int_0^{\infty}\mathrm{j}t\ln s(t)J_a(\zeta t)\,\mathrm{d}t \tag{14}$$

where ζ is a variable of the SFMFBT domain, and $J_a(\zeta t)$ is the αth Bessel function. When $t\in(0,T)$, $s(t)$ can be decomposed into

$$s(t)=\exp\left[\mathrm{j}\sum_{m=1}^{M}C_m J_a\left(\frac{\mu_m t}{kT}\right)\right] \tag{15}$$

where C_m is the mth SFMFBT coefficient, μ_m is the mth ascending positive root of the αth Bessel function, and k is the resolution of Bessel function basis. The calculation formula of C_m can be denoted as

$$C_m=\frac{2\int_0^t\mathrm{j}t\ln s(t)J_\alpha\left(\frac{\mu_m t}{kT}\right)\mathrm{d}t}{\left[kTJ_{\alpha+1}(\mu_m)\right]^2}. \tag{16}$$

Nonetheless, the phase shift ambiguity will occur in (16), which is caused by $\ln s(t)$. We thus replace $\ln s(t)$ using the time frequency ridge in (12) to avoid the phase shift ambiguity. Therefore, we can rewrite (14) and (16) as

$$S_a(\zeta)=\int_0^{\infty}\mathrm{j}ts_{\mathrm{ridge}}(t)J_a(\zeta t)\mathrm{d}t, \tag{17}$$

$$C_m=\frac{2\int_0^t\mathrm{j}ts_{\mathrm{ridge}}(t)J_\alpha\left(\frac{\mu_m t}{kT}\right)\mathrm{d}t}{\left[kTJ_{\alpha+1}(\mu_m)\right]^2}, \tag{18}$$

where $s_{\mathrm{ridge}}(t)$ is the ridge of the time frequency representation. And the formula of C_m can be derived as

$$C_m=\mathrm{j}\frac{-2A_0\mu_m}{J_{\alpha+1}(\mu_m)}\cdot\frac{\sin(kT\omega_0-\phi_m-\theta_0)}{\sqrt{\left(\mu_m^2-k^2T^2\omega_0^2\right)^2+k^2T^2\omega_0^2}} \tag{19}$$

where

$$\phi_m=\arctan\left(\frac{\mu_m^2-k^2T^2\omega_0^2}{kT\omega_0}\right),$$

and $\omega_0=2\pi f_0$. When $\mu_m\to kT\omega_0$, $|C_m|$ get the maximum value. When $|C_m|$ is the maximum, μ_m is recorded as μ_{mmax}. Therefore, the modulation frequency estimation is denoted as

$$\hat{f}_{01}=\frac{\mu_{m\max}}{2\pi kT}. \tag{20}$$

The frequency resolution is shown as

$$\Delta f_k=\frac{\mu_{m+1}}{2\pi kT}-\frac{\mu_m}{2\pi kT}\approx\frac{1}{2kT}. \tag{21}$$

We can see that the introduction of the k-resolution improves the frequency resolution. Based on (21), the modulation frequency can be estimated more precisely. In the following part, we present the complete steps of the modulation frequency estimation.

Step 1 Calculate C_m with (18).

Step 2 Find $\mu_{m\max}$ which maximizes $|C_m|$.

Step 3 Obtain the estimated modulation frequency through (20).

Step 4 Calculate the lower frequency limit $f_L=\hat{f}_{01}-\Delta f_k/2$ and the upper frequency limit $f_H=\hat{f}_{01}+\Delta f_k/2$.

Step 5 For $f\in(f_L,f_H)$, decompose f into L components denoted as f_i. Then we can construct the reference function as

$$s_{\mathrm{ref}}(t)=\sin(2\pi f_i t),\ \ i=1,2,\cdots,L. \tag{22}$$

Then the corresponding modulation frequency estimations $\hat{f}_i=\left\{\hat{f}_1,\hat{f}_2,\cdots,\hat{f}_L\right\}$ can be obtained by performing the SFMFBT on each $s_{\mathrm{ref}}(t)$.

Step 6 The frequency difference f_w will be acquired by averaging the maximum and minimum errors in f_i and $\hat{f}_i$. And the final modulation frequency estimation can be indicated as

$$\hat{f}_0=\hat{f}_{01}-f_m. \tag{23}$$

If the signal contains multiple sinusoidal components, we can first estimate the component with the largest energy and compensate for it. Then find the signal with the second largest energy in the residual signal, and so on, until we find out all the components.

(ii) Maximum frequency offset and modulation initial phase estimation

The basis function is constructed on the parameter space of the maximum frequency offset and the modulation initial phase using the modulation frequency estimation in (23). In the actual signal processing, the received signals are usually discrete. The discrete SFM signal is projected onto the basis function, and these two parameters can be estimated:

$$s(n)=\sigma_0\exp\left\{\mathrm{j}\left[\frac{A_0}{f_0}\sin(2\pi f_0 n+\theta_0)\right]\right\}. \tag{24}$$

The projection can be defined as

$$S(A,\theta)=\sum_{n=0}^{N-1}s(n)\cdot\exp\left\{-\mathrm{j}\left[\frac{A}{\hat{f}_0}\sin\left(2\pi\hat{f}_0 n+\theta\right)\right]\right\},$$
$$n=0,1,\cdots,N-1 \tag{25}$$

where (A,θ) represents the parameter space of the maximum frequency offset and the modulation initial phase. Then, these two parameters are determined by searching the maximum values of

$$\left(\hat{A}_0,\hat{\theta}_0\right)=\arg\max_{A,\theta}|S(A,\theta)|. \tag{26}$$

The flowchart of the method is shown in Fig. 2.

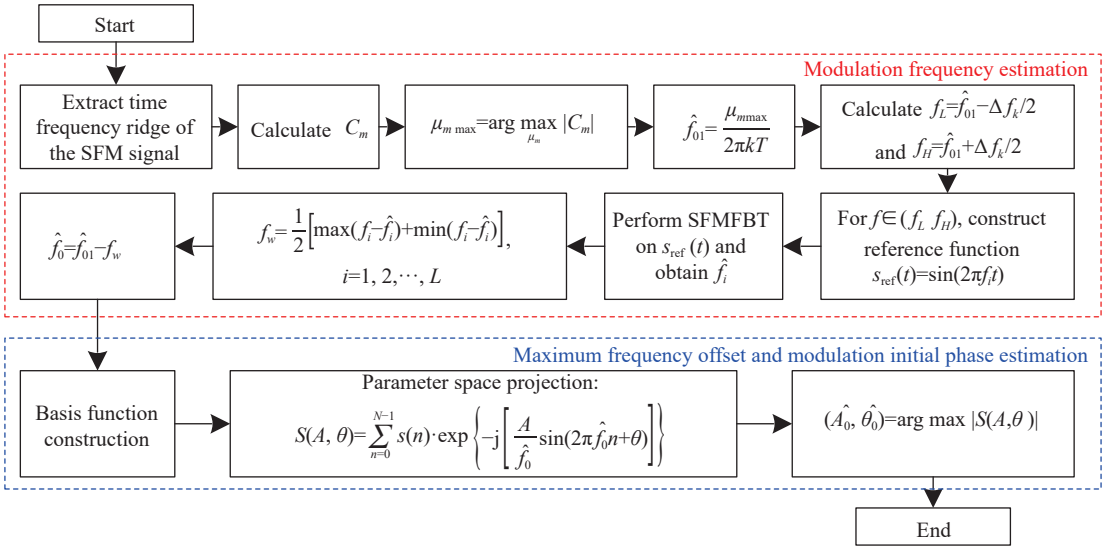

Fig. 2 Flowchart of the proposed algorithm

4. Simulation experiment analysis

4.1 Stationary ship target

First of all, the stationary ship target is modeled in Fig. 3. In addition, the simulation system parameters are shown in Table 1.

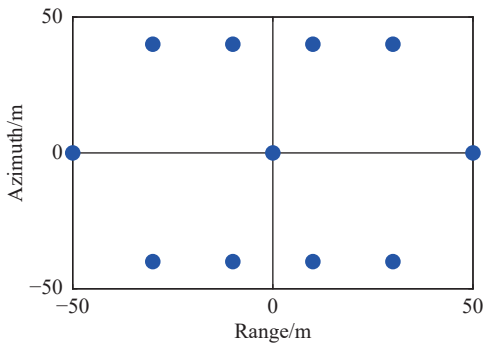

Fig. 3 Stationary ship target model

Table 1 Simulation system parameters

Parameter	Value	Parameter	Value
Carrier frequency/GHz	37.5	Wavelength/m	0.008
Doppler bandwidth/Hz	5 000	Bandwidth/GHz	5
Range resolution/m	0.03	Pulse repetition frequency/Hz	6 250
Azimuth resolution/m	0.04	Pulse width/μs	10
Depression angle/(°)	45	Sampling rate/GHz	6
Synthetic aperture time/s	2.121 3	Platform height/m	3 000
Vibration amplitude/mm	3.959 8	Aircraft speed/(m·s^{-1})	200
Vibration frequency/Hz	20	SNR/dB	10
Vibration initial phase/rad	0	–	–

In order to better extract the time frequency ridge, there should be the dominant scatterer in the scene. It

is worth noting that there can be only one dominant scatterer in a range gate. Through performing the STFT and dechirping the signal via the extended Radon transform (ERT) with the reference of [29], the time frequency ridge is shown in Fig. 4. Then we perform the SFMFBT on part of the time frequency ridge to reduce the computational burden. The SFMFBT coefficient of the time frequency ridge is shown in Fig. 5. Then, we can obtain the frequency estimation via finding the peak.

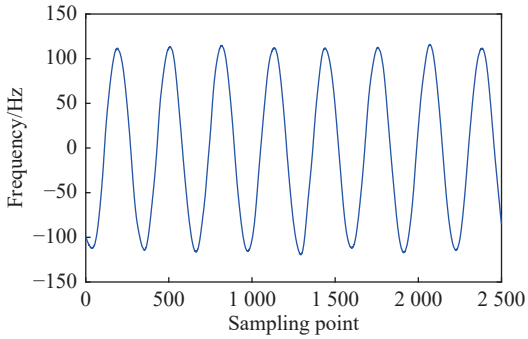

Fig. 4 Time frequency ridge through performing the STFT and dechirping the signal via ERT in [29]

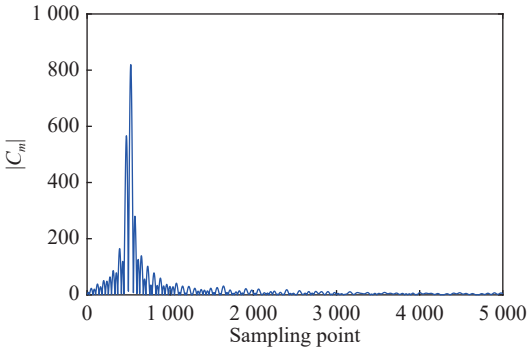

Fig. 5 SFMFBT coefficient of the time frequency ridge

We adopt the DSFMT algorithm mentioned in [11] to contrastively analyze the performance of the proposed method. The parameter estimation results via the DSFMT algorithm in [11] is shown in Fig. 6(a). Contrastively, the estimated results via the SFMFBT algorithm in this paper is shown in Fig. 6(b). Then, we can reconstruct the sinusoidal modulation phase error to construct the compensation function via the SFMFBT algorithm and the parameter space projection. The parameter estimation results of the platform vibration by these two methods are shown in Table 2. Obviously, the SFMFBT algorithm has higher estimation accuracy than the DSFMT algorithm.

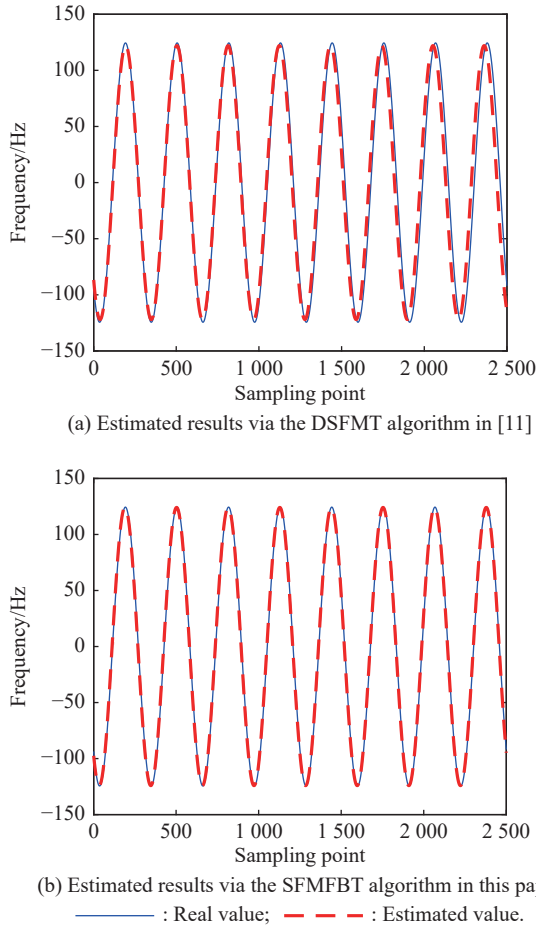

Fig. 6 Results of the parameter estimation

Table 2 Parameter estimation results of the platform vibration via the DSFMT algorithm in [11] and the proposed SFMFBT algorithm

Result		Algorithm	
		DSFMT	SFMFBT
Amplitude	Estimated value/mm	3.848 7	3.940 2
	Relative error/%	2.805 7	0.495 0
Frequency	Estimated value/Hz	20.180 2	19.994 4
	Relative error/%	0.901 0	0.028 0
Initial phase	Estimated value/rad	−0.026 3	−0.019 2
	Absolute error/rad	0.026 3	0.019 2

Finally, the aforementioned compensation function is used for the matched filtering. Then, the time frequency representation without the vibration error compensation is shown in Fig. 7(a). After vibration error compensation, the time frequency representation is shown in Fig. 7(b).

Obviously, the sinusoidal modulation phase error is eliminated perfectly.

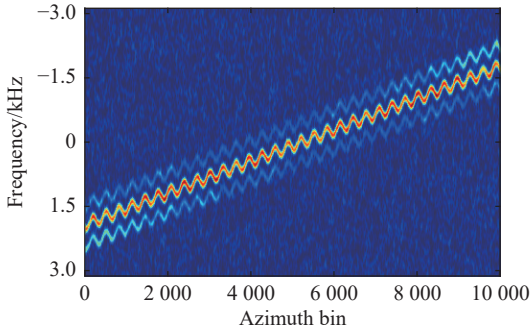

(a) Time frequency representation without high frequency vibration compensation

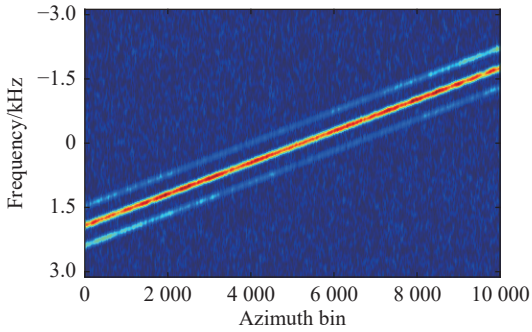

(b) Time frequency representation after high frequency vibration compensation via the SFMFBT algorithm

Fig. 7 Time frequency representations of a certain range cell after range compression

After the phase error removal, the RD technique is used to obtain the final imaging results. The azimuth profiles before and after the SFMFBT are shown in Fig. 8, where the extension along the azimuth dimension is well suppressed via the vibration compensation. The imaging result before vibration error compensation is shown in Fig. 9.

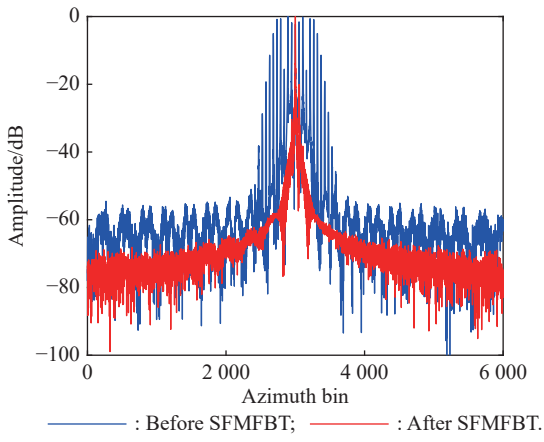

Fig. 8 Azimuth profiles before and after SFMFBT

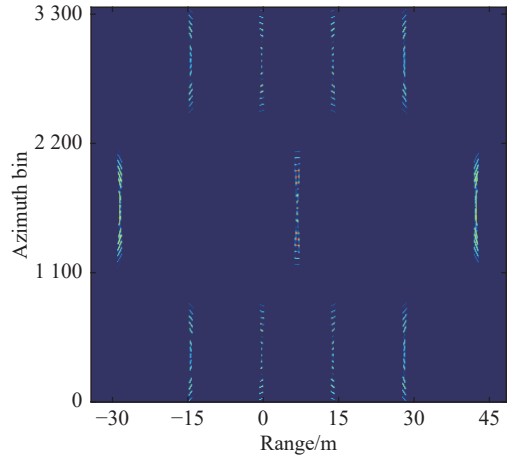

Fig. 9 SAR imaging result before vibration error compensation

We perform the DSFMT algorithm in [11] and the SFMFBT algorithm to compensate for the platform vibration error respectively. The SAR imaging results obtained via the DSFMT algorithm and the SFMFBT algorithm are shown in Fig. 10(a) and Fig. 10(b) respectively. Obviously, the DSFMT algorithm in [11] can also suppress the paired echoes, but its imaging effect is inferior to that of the SFMFBT algorithm. The paired echoes are suppressed significantly and the ship target is clearly visible after the vibration compensation in Fig. 10(b). In addition, we use the image entropy shown in Table 3 to prove the improvement of the image quality. It is obvious that the SFMFBT algorithm has better performance than the DSFMT algorithm. In addition, the reduction of the image entropy based on the SFMFBT algorithm demonstrates the validity of the proposed method.

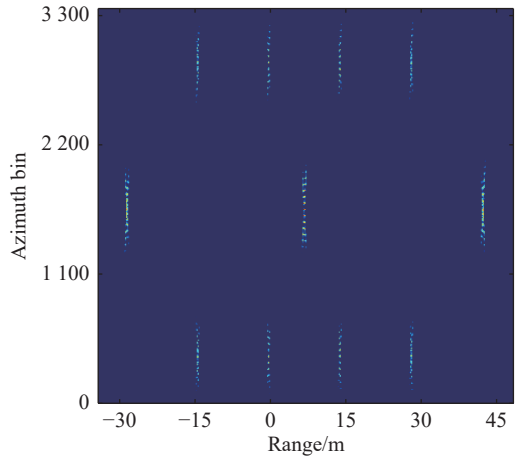

(a) SAR image after platform vibration compensation via the DSFMT algorithm in [11]

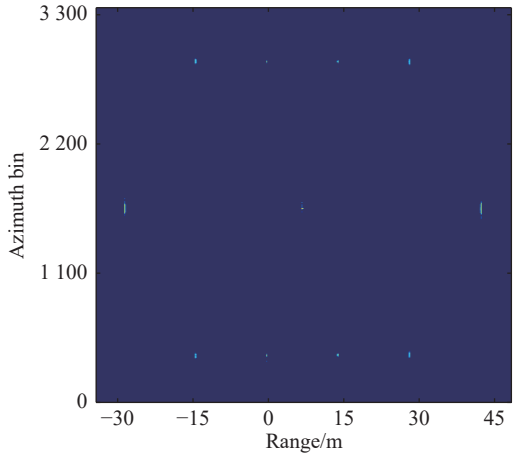

(b) SAR image after platform vibration compensation via the SFMFBT algorithm in this paper

Fig. 10 SAR imaging results after platform vibration compensation

Table 3 Image entropy of SAR imaging results

Figure	Image entropy
Fig. 9	11.2988
Fig. 10(a)	10.5643
Fig. 10(b)	8.5972

The SFMFBT proposed in this paper focuses on the vibration frequency estimation, whose precision directly affects the image quality after compensation. To further illustrate the performance of the SFMFBT algorithm, the simulations are presented at various SNRs. It is worth noting that the SNR is defined in the raw echo data. Meanwhile, the estimated values and the relative errors of the vibration frequency are shown in Table 4. We can see that the estimation error of the vibration frequency gradually decreases with the increase of SNR.

Table 4 Estimated values and relative errors of the vibration frequency via the SFMFBT algorithm

SNR/dB	Estimated value/Hz	Relative error/%
−10	19.8598	0.7010
−5	19.8654	0.6730
0	19.9640	0.1800
5	20.0165	0.0825
10	19.9944	0.0280

4.2 Ship target with translational and rotational movement

In practice, the motion of ship target at sea is complicated. Thus, in this section, we consider the ship target animated by the translational and rotational movement. The translation parameters are shown in Table 5, and the rotation parameters are shown in Table 6. The simulated parameters in Table 1 and the model in Fig. 3 are also adopted.

Table 5 Translation parameters of the ship target

Velocity/(m·s^{-1})	Direction/(°)
2	0

Table 6 Rotation parameters of the ship target

Dimensionality	Amplitude/(°)	Average period/s
Roll	2.500	26.4
Pitch	0.450	11.2
Yaw	0.665	33.0

Similarly, there should be the dominant scatterer in the scene. As shown in Fig. 11, the time frequency ridge is obtained through performing the STFT and dechirping the signal via the ERT in [29]. Obviously, the signal in Fig. 11 is periodic with both high frequency and low frequency, which are caused by the platform vibration and the ship target motion respectively. Then, the SFMFBT algorithm and the parameter space projection proposed in Section 3 are employed for the parameter estimation and the phase error is reconstructed for the compensation function construction. The SFMFBT coefficient of the time frequency ridge is shown in Fig. 12, We can find out a peak to estimate the frequency vibration.

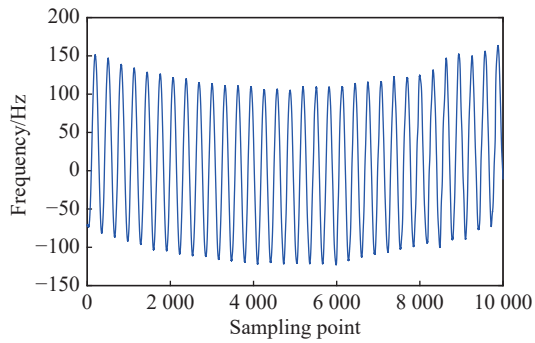

Fig. 11 Time frequency ridge through performing the STFT and dechirping the signal via ERT in [29]

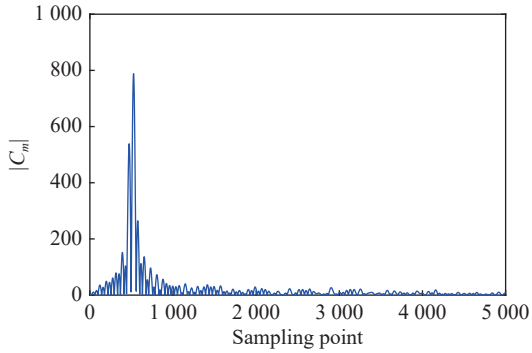

Fig. 12 SFMFBT coefficient of the time frequency ridge

The results of the parameter estimation are shown in Fig. 13, where Fig. 13(a) is based on the DSFMT algorithm in [11] while Fig. 13(b) is based on the SFMFBT algorithm. Similarly, only part of the time frequency ridge is used for the parameter estimation. The parameter estimation results of the platform vibration via the DSFMT algorithm in [11] and the SFMFBT algorithm are shown in Table 7. It is clear that the SFMFBT algorithm has higher estimation accuracy than the DSFMT algorithm.

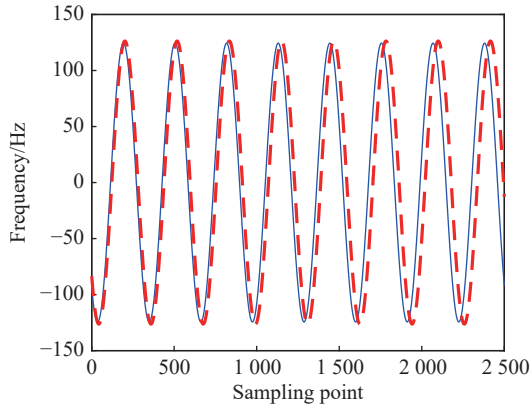

(a) Estimated results via the DSFMT algorithm in [11]

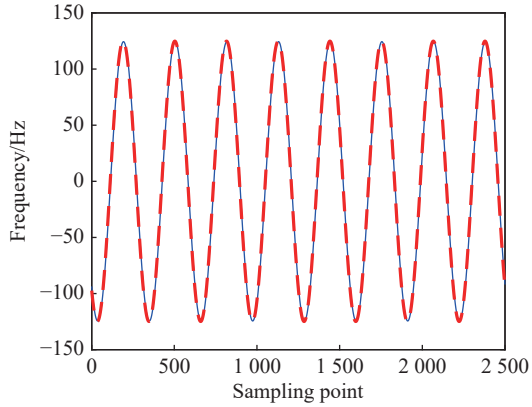

(b) Estimated results via the SFMFBT algorithm in this paper

——— : Real value; — — — : Estimated value.

Fig. 13 Results of the parameter estimation

Table 7 Parameter estimation results of the platform vibration via the DSFMT algorithm in [11] and the proposed SFMFBT algorithm

Value		Algorithm	
		DSFMT	SFMFBT
Amplitude	Estimated values/mm	4.0684	3.9752
	Relative error/%	2.7426	0.3889
Frequency	Estimated values/Hz	19.7600	19.9944
	Relative error/%	1.2000	0.0280
Initial phase	Estimated values/rad	−0.1745	0.0410
	Absolute error/rad	0.1745	0.0410

Finally, the compensation function is constructed for the platform vibration compensation. The time frequency representation without the vibration error compensation is shown in Fig. 14(a), and the time frequency representation after the vibration error compensation is shown in Fig. 14(b). Obviously, the phase error is eliminated perfectly.

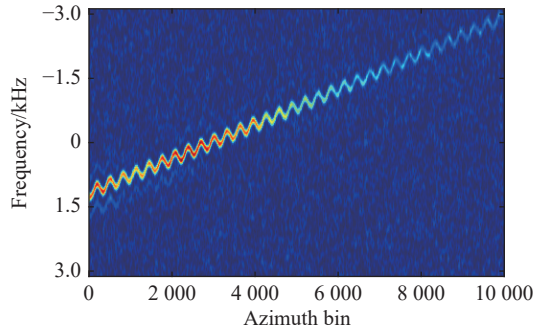

(a) Time frequency representation without high frequency vibration compensation

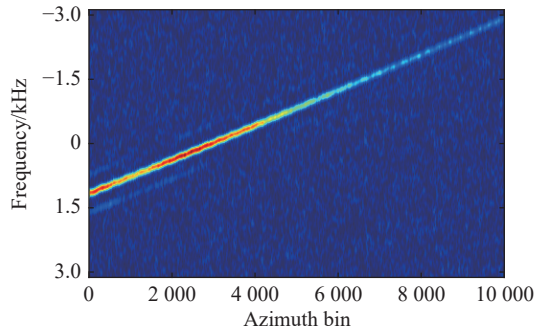

(b) Time frequency representation after high frequency vibration compensation via the SFMFBT algorithm

Fig. 14 Time frequency representations of a certain range cell after range compression

By using the RD technique, the azimuth profiles before and after the platform vibration compensation are shown in Fig. 15, where the extension along the azimuth dimension is well suppressed through the high frequency vibration compensation based on the SFMFBT algorithm. The SAR imaging result before the motion compensation is shown in Fig. 16.

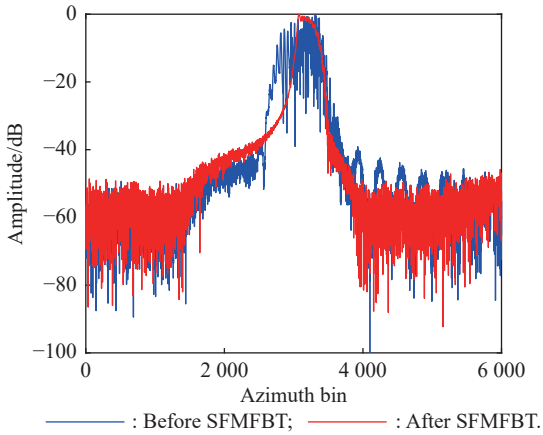

Fig. 15 Azimuth profiles before and after SFMFBT

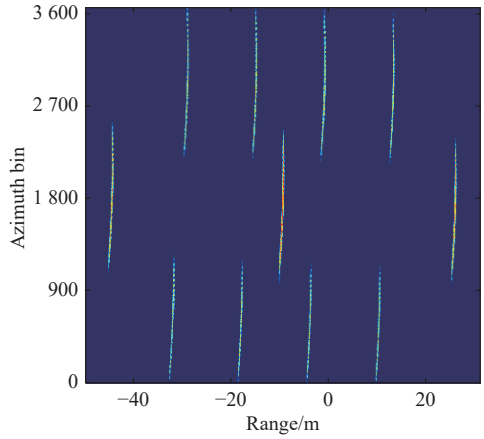

Fig. 16 SAR imaging result without motion compensation

After the platform vibration compensation, the imaging results based on the DSFMT algorithm in [11] and the SFMFBT algorithm are shown in Fig. 17(a) and Fig. 17(b) respectively. Obviously, the paired echoes introduced by the platform vibration is not completely compensated in Fig. 17(a), but it is suppressed well in Fig. 17(b). Consequently, we select the proposed SFMFBT algorithm for the platform vibration compensation.

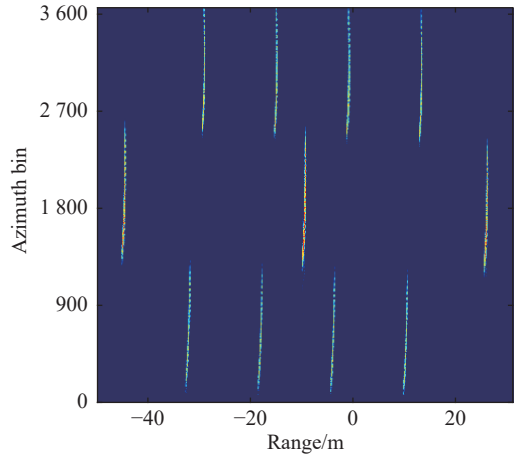

(a) SAR image after platform vibration compensation via the DSFMT algorithm in [11]

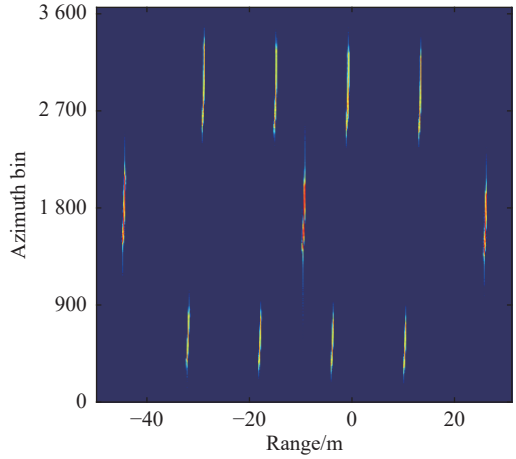

(b) SAR image after platform vibration compensation via SFMFBT algorithm in this paper

Fig. 17 SAR imaging results after platform vibration compensation

Due to the motion of the ship target, the imaging results after the platform vibration compensation is still defocused. Hence, the inverse SAR (ISAR) refocusing technique proposed in [30] is adopted for further focus.

The final imaging result after the SFMFBT-based platform vibration compensation and the ISAR refocusing technique is shown in Fig. 18. Obviously, the defocus introduced by the platform vibration and the motion of ship target is suppressed perfectly via the proposed approach.

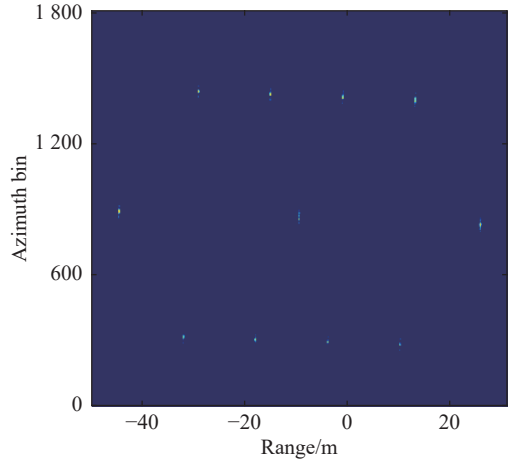

Fig. 18 Final imaging result after the SFMFBT-based platform vibration compensation and the ISAR refocusing technique

As shown in Table 8, the image entropy is adopted to further illustrate the imaging quality. It is clear that the effect of the platform vibration compensation based on the DSFMT algorithm in [11] is inferior to that of the SFMFBT algorithm. The reduction of the image entropy illustrates the improvement of the imaging quality. There-

fore, the validity and the high precision of the proposed method are proved.

Table 8 Image entropy of SAR imaging results

Figure	Image entropy
Fig. 16	11.9644
Fig. 17(a)	11.8153
Fig. 17(b)	11.5594
Fig. 18	7.8738

Then, we present the simulations at various SNRs to demonstrate the performance of the SFMFBT algorithm. Similarly, the SNR is defined in the raw echo data. Simultaneously, the estimated values and the relative errors of the vibration frequency are shown in Table 9. It is clear that the estimation error of the vibration frequency gradually decreases with the increase of SNR. The purpose of Table 4 and Table 9 is to illustrate the relationship between the vibration frequency estimation accuracy and the SNR, and the statistical analysis is not performed.

Table 9 Estimated values and the relative errors of the vibration frequency via the SFMFBT algorithm

SNR/dB	Estimated value/Hz	Relative error/%
−10	20.1109	0.5545
−5	20.0986	0.4930
0	20.0165	0.0825
5	20.0140	0.0700
10	19.9944	0.0280

5. Conclusions

In the ultrahigh resolution SAR systems, the high frequency vibration cannot be ignored, which can severely deteriorate the image quality. In this paper, the SFMFBT in conjunction with the time frequency ridge extraction and parameter space projection is presented for the vibration parameter estimation. This proposed method has high estimation precision, and the phase error can be compensated significantly. Compared with the traditional motion compensation technique, the proposed method has the ability to accurately reconstruct the phase error introduced by the high frequency vibration and obtain the well-focused imaging results. Finally, the simulated data for the ship target's radar return demonstrates the validity and the high precision of the proposed method. However, in practice, platform vibrations are more complicated, so the further research for the vibration with multiple frequencies will be studied.

References

[1] XIONG X Y, LI G, MA Y H, et al. New slant range model and azimuth perturbation resampling based high-squint maneuvering platform SAR imaging. Journal of Systems Engineering and Electronics, 2021, 32(3): 545–558.
[2] FANG J, HU S H, MA X L. SAR image de-noising via grouping-based PCA and guided filter. Journal of Systems Engineering and Electronics, 2021, 32(1): 81–91.
[3] FANG F, HE R R, XU W, et al. Study on precise satellite attitude maneuvering strategy for ultrahigh resolution spaceborne SAR imaging. IEEE Access, 2021, 9: 127226–127239.
[4] JIN Y H, CHEN J L, XIA X G, et al. Ultrahigh-resolution autofocusing for squint airborne SAR based on cascaded MD-PGA. IEEE Geoscience and Remote Sensing Letters, 2022, 19: 4017305.
[5] LIN H, CHEN J L, XING M D, et al. Time-domain autofocus for ultrahigh resolution SAR based on azimuth scaling transformation. IEEE Trans. on Geoscience and Remote Sensing, 2022, 60: 527812.
[6] SHI H Y, ZHOU Q X, YANG X Y, et al. SAR imaging method for sea scene target based on improved phase retrieval algorithm. Journal of Systems Engineering and Electronics, 2016, 27(6): 1176–1182.
[7] HUANG Z W, HE Z H, SUN Z Y, et al. Analysis and compensation of vibration error of high frequency synthetic aperture radar. Proc. of the IEEE International Geoscience and Remote Sensing Symposium, 2016: 1138–1141.
[8] SUN W, SUN J P, ZHANG Y, et al. Terahertz ViSAR vibration compensation imaging algorithm for large strabismus helicopter. Journal of Beijing University of Aeronautics and Astronautics, 2016, 42(12): 2755–2761.
[9] WANG H, ZHANG Y, WANG B B, et al. A novel helicopter-borne terahertz SAR imaging algorithm based on Keystone transform. Proc. of the 12th International Conference on Signal Processing, 2014: 1958–1962.
[10] XIA H T, CHEN Q, LI Y W, et al. A high frequency vibration compensation approach in terahertz SAR based on wavelet multi-resolution analysis. Proc. of the China International SAR Symposium, 2018: 10796–10803.
[11] WANG Y, WANG Z F, ZHAO B, et al. Enhancement of azimuth focus performance in high-resolution SAR imaging based on the compensation for sensors platform vibration. IEEE Sensors Journal, 2016, 16(16): 6333–6345.
[12] LI Y W, WU Q, WU J W, et al. Estimation of high-frequency vibration parameters for terahertz SAR imaging based on FrFT with combination of QML and RANSAC. IEEE Access, 2021, 9: 5485–5496.
[13] LI Y W, DING L, ZHENG Q B, et a. A novel high-frequency vibration error estimation and compensation algorithm for THz-SAR imaging based on local FrFT. Sensors, 2020, 20(9): 2669.
[14] SHI S Y, LI C, HU J M, et al. A high frequency vibration compensation approach for terahertz SAR based on sinusoidal frequency modulation fourier transform. IEEE Sensors Journal, 2021, 21(9): 10796–10803.
[15] SHI S Y, LI C, HU J M, et al. Motion compensation for terahertz synthetic aperture radar based on subaperture decomposition and minimum entropy theorem. IEEE Sensors Journal, 2020, 20(24): 14940–14949.
[16] DENG B, LI X, WANG H Q, et al. Theories & methods for SAR micro-motion target detection and imaging. Beijing: Science Press, 2014.
[17] ZHANG Y, SUN J P, LEI P, et al. SAR-based paired echo

focusing and suppression of vibrating targets. IEEE Trans. on Geoscience and Remote Sensing, 2014, 52(12): 7593–7605.
[18] XIA W J, HUANG L L. Target vibration estimation in SAR based on phase-analysis method. Eurasip Journal on Advances in Signal Processing, 2016, 2016: 94.
[19] PENG B, WEI X Z, DENG B, et al. A sinusoidal frequency modulation fourier transform for radar-based vehicle vibration estimation. IEEE Trans. on Instrumentation and Measurement, 2014, 63(9): 2188−2199.
[20] YANG Q, DENG B, WANG H Q, et al. Parameter estimation and image reconstruction of rotating targets with vibrating interference in the terahertz band. Journal of Infrared Millimeter and Terahertz Waves, 2017, 38(7): 909–928.
[21] WANG Q, PEPIN M, WRIGHT A, et al. Reduction of vibration-induced artifacts in synthetic aperture radar imagery. IEEE Trans. on Geoscience and Remote Sensing, 2014, 52(6): 3063–3073.
[22] WANG Q, PEPIN M, BEACH R, et al. SAR-based vibration estimation using the discrete fractional fourier transform. IEEE Trans. on Geoscience and Remote Sensing, 2012, 50(10): 4145–4156.
[23] LIANG Y, LI G F, ZHANG G, et al. A nonparametric paired echo suppression method for helicopter-borne SAR imaging. IEEE Geoscience and Remote Sensing Letters, 2020, 17, (12): 2080−2084.
[24] LIU Q X, HE F. Adaptive image formation algorithm for THz-SAR based on automatic motion compensation. Proc. of the IEEE Asia-Pacific Conference on Antennas and Propagation, 2018: 179−180.
[25] LATHI B P. Signal processing & linear systems. Cary: Oxford University Press, 1998.
[26] ZHAO Y L, ZHANG Q Y, C, LI C, et al. Vibration error analysis and motion compensation of video synthetic aperture radar. Journal of Radars, 2015, 4(2): 230–239. (in Chinese)
[27] ZHANG X C, ZHANG Y X, SUN J P. Effects analysis of helicopter platform vibration on terahertz SAR imaging. Journal of Terahertz Science and Electronic Information Technology, 2018, 16(2): 205−211.
[28] HE Q F, ZHANG Q, LUO Y et al. A sinusoidal frequency modulation Fourier-Bessel transform and its application to micro-Doppler feature extraction. Journal of Radars, 2018, 7(5): 593−601. (in Chinese)
[29] WANG Z F, WANG Y, XU L. Parameter estimation of hybrid linear frequency modulation-sinusoidal frequency modulation Signal. IEEE Signal Processing Letters, 2017, 24(8): 1238−1241.
[30] CAO R, WANG Y, ZHAO B, et al. Ship target imaging in airborne SAR system based on automatic image segmentation and ISAR technique. IEEE Journal of Selected Topics in Applied Earth Observations and Remote Sensing, 2021, 14: 1985−2000.

Biographies

CHEN Siyu was born in 1999. She received her B.S. degree in 2021 from Harbin Institute of Technology (HIT), Harbin, China. She is pursuing her Ph.D. degree in information and communication engineering from HIT. Her current research interests are signal processing and SAR imaging.
E-mail: 21b905043@stu.hit.edu.cn

WANG Yong was born in 1979. He received his B.S. and M.S. degrees from Harbin Institute of Technology (HIT), Harbin, China, in 2002 and 2004, respectively, both in electronic engineering. He received his Ph.D. degree in information and communication engineering from HIT in 2008. He is a professor with the Institute of Electronic Engineering Technology in HIT. He was elected in the Program for New Century Excellent Talents in University of Ministry of Education of China in 2012, and received the Excellent Doctor's Degree Nomination Award in China in 2010. His main research interests are time frequency analysis of nonstationary signal, radar signal processing, and their application in synthetic aperture radar imaging.
E-mail: wangyong6012@hit.edu.cn

CAO Rui was born in 1996. She received her B.S. degree in electronic information engineering and M.S. degree in 2018, in information and communication engineering and from Harbin Institute of Technology (HIT), Weihai, China, in 2020. She is pursuing her Ph.D. degree in information and communication engineering from HIT, Harbin, China. Her current research interests include radar imaging and signal processing.
E-mail: caor@hit.edu.cn